

Thermal Field Measurements for a Shaped Hole at Low and High Freestream Turbulence Intensity

Robert P. Schroeder¹

Department of Mechanical
and Nuclear Engineering,
The Pennsylvania State University,
University Park, PA 16802
e-mail: rschroeder@sargentlundy.com

Karen A. Thole

Department of Mechanical
and Nuclear Engineering,
The Pennsylvania State University,
University Park, PA 16802
e-mail: kthole@psu.edu

Shaped holes are increasingly selected for airfoil cooling in gas turbines due to their superior performance over that of cylindrical holes, especially at high blowing ratios. The performance of shaped holes is regarded to be the result of the diffused outlet, which slows and laterally spreads coolant, causing coolant to remain close to the wall. However, few thermal field measurements exist to verify this behavior at high blowing ratio or to evaluate how high freestream turbulence alters the coolant distribution in jets from shaped holes. The present study reports measured thermal fields, along with measured flowfields, for a shaped hole at blowing ratios up to three at both low and high freestream turbulence intensities of 0.5% and 13.2%. Thermal fields at low freestream turbulence intensity showed that the coolant jet was initially attached, but far downstream of the hole the jet lifted away from the surface due to the counter-rotating vortex pair. Elevated freestream turbulence intensity was found to cause strong dilution of the coolant jet and also increased dispersion, almost exclusively in the lateral as opposed to the vertical direction. Dominance of lateral dispersion was due to the influence of the wall on free-stream eddies, as indicated from changes in turbulent shear stress between the low and high freestream turbulence cases. [DOI: 10.1115/1.4034798]

Introduction

With combustion temperatures far exceeding the melting temperature of metal components in gas turbines, film cooling holes are critical for maintaining parts at acceptable service temperature. Cooling designers often use shaped holes, owing to how shaped holes promote jet attachment and exhibit adiabatic effectiveness that only gradually varies with blowing ratio [1]. At high coolant flow rates, shaped holes can deliver satisfactory performance whereas jets from cylindrical holes are fully detached [2]. Recent studies indicate interest in shaped hole performance at high coolant flow rates: adiabatic effectiveness for shaped holes is reported by Heneka et al. [3] up to $M = 3.0$ ($I = 6.0$) and by Colban et al. [4] up to $M = 4.0$ ($I = 8.0$). However, corresponding measurements of thermal field at high blowing ratio have not been made to investigate performance of these shaped hole jets. Little is known about the distribution of coolant within these jets, especially for cases with high freestream turbulence intensity that is characteristic of flow exiting the gas turbine combustor.

The present study reports thermal fields measured for shaped holes at high blowing ratio. First, thermal fields are presented for a condition of low freestream turbulence intensity, $Tu_\infty = 0.5\%$. Comparison is made to flowfield data to gain insight into behavior of the shaped hole jet. Then thermal field and flowfield data are presented for high freestream turbulence intensity of $Tu_\infty = 13.2\%$. Jet behavior is again discussed. Differences in how coolant disperses at low and at high freestream turbulence intensity are explained. As well as illuminating behavior of shaped hole jets, data of the present study are useful for validating film-cooling computational fluid dynamics models at quiescent and at highly turbulent freestream conditions.

Previous Studies

Thermal field studies of film cooling flows provide insights not available from the surface measurements alone. For example, Thole et al. [2] measured thermal fields in the centerline plane of

cylindrical holes and observed the different trajectories of jets over a range of density ratios and coolant flow rates. From the thermal fields, they identified three regimes of jet-trajectory behavior for cylindrical holes: attached ($I < 0.4$), initially detached but then reattaching downstream ($0.4 < I < 0.8$), and fully detached downstream of the hole ($I > 0.8$).

Thermal field measurements with shaped holes are rare. Kohli and Bogard [5] reported thermal fields for shaped holes with steep injection angle ($\alpha = 55^\circ$) at blowing ratios up to $M = 0.8$. They observed mainstream ingestion into the diffused outlets, but performance was still superior to cylindrical holes because coolant was spread laterally by the diffused outlets. Takeishi et al. [6] used planar laser-induced fluorescence to measure thermal fields for shaped holes at blowing ratios up to $M = 1.5$ and likewise observed instances of mainstream ingestion. They also observed increased coolant penetration into the mainstream with increased blowing ratio, with the coolant jet detaching at the shaped hole trailing edge in one instance. Funazaki et al. [7] reported thermal fields at $M = 0.5$ and 1.0 for shaped holes with and without protrusions on the film-cooled surface upstream of the holes. Protrusions were shown to cause slight coolant dilution but also increased lateral spreading of coolant close to the wall. All these shaped hole studies were performed with low freestream turbulence intensity.

While thermal field measurements at high freestream turbulence have not been previously reported for shaped holes, the authors are aware of two experimental studies on cylindrical holes. Kohli and Bogard [8] measured the fluctuating thermal field for $M = 0.4$ jets from cylindrical holes with freestream turbulence of 20% and found that the high freestream turbulence “obliterated” the jet-mainstream interface. Mainstream fluid intermittently penetrated through the coolant jet to the wall, and conversely some coolant was ejected from the jet into the mainstream. Cutbirth and Bogard [9] measured time-mean thermal fields for compound-angle cylindrical holes on a vane pressure side with turbulence intensity of 20% at the cascade inlet. They observed the elevated freestream turbulence caused unsteady lateral oscillation (displacement) of the coolant jet rather than increased dispersion of the coolant jet. Correspondingly, flow field measurements showed that turbulence surrounding the coolant jet was dominated by fluctuations in the lateral velocity component.

¹Present address: Sargent and Lundy, Chicago, IL 60603.

Contributed by the International Gas Turbine Institute (IGTI) of ASME for publication in the JOURNAL OF TURBOMACHINERY. Manuscript received August 16, 2016; final manuscript received September 1, 2016; published online November 2, 2016. Editor: Kenneth Hall.

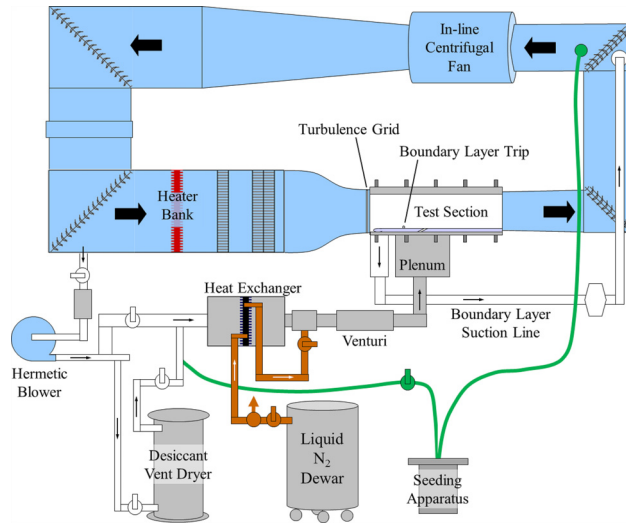


Fig. 1 Schematic of the film cooling wind tunnel

To add to this thermal field literature, the present study reports thermal fields for a baseline, publicly available shaped hole design [10]. Measurements were performed at high blowing ratios up to $M = 3$ and were performed at both low and high freestream turbulence intensities. To provide a comprehensive understanding, thermal field data are complemented by previously measured flow field data [11] at the same conditions. Besides adding to our understanding of shaped hole performance, data of the present study are useful for benchmarking of computational fluid dynamics simulations and qualification of new film cooling experimental facilities.

Experimental Facility and Methods

The recirculating wind tunnel shown in Fig. 1 was used for experiments with the baseline-shaped hole [10]. Mainstream test section air was driven by an in-line centrifugal fan and air temperature was conditioned by a chilled water heat exchanger and an electric heater bank. Air flowed through a 6:1 contraction to enter the test section featuring a flat-plate floor with a row of five shaped holes. Test section conditions were maintained at 295 K and 10 m/s mainstream velocity.

To control the boundary layer over the flat plate, a suction loop was used to remove the incoming boundary layer so that a new boundary layer developed from the plate leading edge. A trip wire at $x/D = -33$ caused transition to a turbulent boundary layer. Per boundary layer profiles previously reported by Schroeder and Thole [11], the boundary layer was fully turbulent at $x/D = -2$. Table 1 provides characterization of the mainstream approach boundary layer.

Tests were performed at two freestream turbulence intensities in this study, $Tu_\infty = 0.5\%$ and 13.2% . Turbulence intensities are reported for the $x/D = -2$ location. The low intensity of $Tu_\infty = 0.5\%$ was obtained without a turbulence grid installed in the wind tunnel. High freestream turbulence intensity of $Tu_\infty = 13.2\%$ was obtained by precisely positioning a passive grid of vertical bars near the test section entrance at $x/b = -14$, where bar diameter was $b = 38$ mm. Bars were spaced apart $2b$ center-to-center. As

Table 1 Boundary layer characteristics

Tu_∞	δ_2/D	H	Re_{δ_2}	$c_f/c_{f,0}$
0.5%	0.14	1.45	670	1.0
13.2%	0.12	1.38	580	1.19

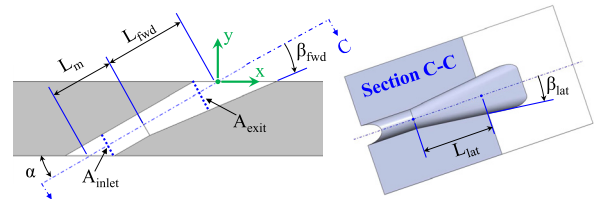


Fig. 2 Shaped hole geometry

Table 2 Geometric parameters of the shaped hole

P/D	6	L_m/D	2.5
α	30 deg	$L_{lat}/D, L_{fwd}/D$	3.5
β_{fwd}, β_{lat}	7 deg	Area ratio, AR	2.5

measured by hot wire, the integral length scale of the $Tu_\infty = 13.2\%$ turbulence was $\Lambda_x = 5.2D$ at the shaped hole trailing edge.

The supply loop for the film cooling flow is shown at the bottom of Fig. 1. Air for coolant was withdrawn from the wind tunnel far upstream of the test section and was driven by a hermetically sealed blower through a heat exchanger to cool the air using liquid nitrogen. Coolant flow rate was measured by a Venturi flowmeter and then coolant flowed up through a plenum with fine screens to be evenly distributed to entrances of the five shaped holes. All experiments were performed at the density ratio $DR = 1.5$, which necessitated strategies to avoid frost formation on cold surfaces. Prior to experiments, all wind tunnel air was dried by routing it through the desiccant vent dryer branch of the coolant loop. Also, during experiments, a separate pipeline was used to keep the wind tunnel positively pressurized with nitrogen gas.

The shaped holes used in this study were those introduced as baseline geometry by Schroeder and Thole [10]. Computer-aided design models and performance data for these holes are publicly available for download at the authors' website.² Geometry of this hole is shown in Fig. 2 and geometric parameters are listed in Table 2. Expansion angles of the shaped hole were 7 deg in each of the three directions from the metering-section centerline. Metering diameter was $D = 7.75$ mm.

The flat plate material in which the shaped holes were machined was styrofoam residential sheathing (polystyrene). Polystyrene was the preferred material for adiabatic effectiveness measurements and thermal field measurements due to its low conductivity of $k = 0.029$ W/m-K. The test plate material remained the same for flowfield measurements.

Adiabatic Effectiveness Measurements. Adiabatic wall temperatures were measured and nondimensionalized in effectiveness (η) levels using an infrared camera. The infrared camera viewed the film-cooled surface through a ZnSe window in the test section ceiling. To ensure that temperatures were accurately detected for the entire range of surface temperatures, camera output was calibrated to thermocouples on the test plate surface similar to as done by Eberly and Thole [12]. The calibration was applied to infrared images to obtain the adiabatic wall temperature. Free-stream and coolant temperatures were both averages of multiple thermocouples in the respective locations (mainstream, and coolant plenum $2.5D$ below entrances to film cooling holes).

Thermal Field Measurements. The time-mean thermal field (θ) was measured using a specially designed thermocouple rake. The thermal field was measured in three planes: the centerline x - y plane and the y - z crossplanes at $x/D = 4$ and 10. Thermocouples on the rake had wire diameter of 0.05 mm and junction diameter

²<http://www.mne.psu.edu/psuturbine>

of approximately 0.12 mm. Heat leak down the wires was minimized based on a conductive analysis of the probes. Error in thermocouple readings due to heat leak along wires was estimated to be less than $|\Delta\theta| = 0.05$, based on numerical simulations of a 1D thermocouple model. Temperatures were the time-mean of at least 36,000 samples taken over at least 30 s for each measurement location, which was verified in each case to provide converged values of θ .

Flowfield Measurements. Particle image velocimetry (PIV) was used to measure flowfields in two planes of the flow: the centerline x - y plane and the y - z crossplane at $x/D = 4$. These planes and their respective PIV setups are illustrated in Figs. 3(a)–3(b). Note that PIV measurements were made in the same manner as previously reported [11]. For both setups in the present study, mainstream and coolant were equally seeded with di-ethyl-hexyl-sebacate (DEHS) droplets that followed the flow due to their low Stokes number (maximum $Stk = 0.010$). A dual-head Nd:YLF laser illuminated the respective measurement planes and high-speed CMOS cameras captured image pairs of the illuminated particles.

For PIV in the centerline plane, images were obtained using a single camera viewing normal to measurement plane as shown in Fig. 3(a). Image pairs were recorded at 4 kHz with image size of 1024×256 pixels. Time-mean flowfields were calculated over at least 8000 time instants spread over a period of 2 s, which corresponded to more than 240 flow crossings of the PIV field of view ($x/D = -2$ to 8.6). Time delay between laser pulses was chosen to provide particle displacements around eight pixels in the image pairs. Particle displacements, and thereby velocities, were calculated with commercial software [13] using a multipass scheme of interrogation windows ending with final window size of 16×16 pixels and 75% overlap. This final window size corresponded to $0.18D \times 0.18D$ since spatial resolution was 11.6 pixels/mm. Background subtraction, intensity normalization, and universal outlier detection were all implemented.

A stereo PIV setup was used to measure flowfields in the $x/D = 4$ crossplane. This setup, shown in Fig. 3(b), used perspective views from two cameras to measure all three components of velocity. Scheimpflug lens adapters brought the measurement plane into focus for each camera. Image pairs were recorded at 250 Hz on each camera with image size of 1024×512 pixels. Time-mean flowfields were calculated over at least 4000 time instants spread over a period of 16 s. Time delay between laser pulses was set between 22 and $26 \mu s$ to obtain particle displacements around four pixels in the dewarped images used to compute vectors. Velocities were calculated [13] using a multipass scheme of interrogation windows ending in 32×32 pixel interrogation windows with 50% overlap. Final window size corresponded to $0.19D \times 0.19D$ since the spatial resolution was 21.9 pixels/mm. Intensity normalization and universal outlier detection were used for calculating velocities in the $x/D = 4$ crossplane.

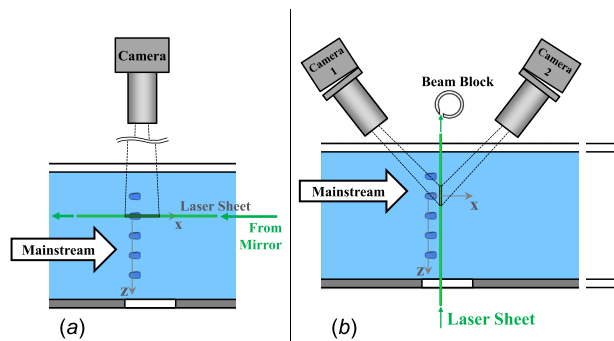


Fig. 3 Measurement setups for (a) PIV in the centerline plane and (b) stereo PIV in the $x/D = 4$ crossplane

Uncertainty Analysis. Uncertainty was calculated for all measurements. Propagation of uncertainty was estimated using the partial derivatives method of Figliola and Beasley [14] and values are reported for a 95% confidence interval. Regarding test conditions, maximum uncertainty in density ratio was ± 0.04 . For blowing ratio, the uncertainty was dominated by bias uncertainty of the Venturi flowmeter and variation during thermal field measurements. Uncertainty was higher at lower blowing ratios. Maximum uncertainty in $M = 1.5$ was $\pm 6.5\%$.

For adiabatic effectiveness, uncertainty was driven by uncertainty in the coolant temperature and in the plate surface temperature. Adiabatic effectiveness uncertainty was calculated to be $\delta\eta = \pm 0.025$. Analogously, major contributors to thermal field uncertainty were the uncertainties in coolant temperature and in temperature measured by the thermocouple rake, as well as heat leak down the thermocouple wires. Including a representative heat leak error of $\Delta\theta = -0.035$, maximum uncertainty was calculated to be $\delta\theta = \pm 0.048$. Repeatability checks of thermal field profiles agreed within this uncertainty, as shown in Fig. 4.

For PIV flowfield measurements, both the bias and precision uncertainties were considered. Bias uncertainties were estimated by assuming a displacement bias uncertainty of ± 0.15 pixels, which translated to velocity bias uncertainty of $\pm 1.9\%$ in the centerline plane and $\pm 4.8\%$ in the $x/D = 4$ crossplane. Precision uncertainties were estimated from repeatability tests in the centerline plane and were combined with bias uncertainty to estimate overall uncertainties in individual components of mean velocity. Overall uncertainty of U was estimated to be $\pm 4.5\%$ and $\pm 6.3\%$ in the centerline plane and crossplane, respectively, with percentages based on U_∞ . Overall uncertainty of V (and of W) was similarly estimated to be $\pm 2.5\%$ and $\pm 5.1\%$ in those same respective planes. Repeatability tests in the centerline plane were also used to estimate precision uncertainties for rms velocities and turbulent shear stresses. Uncertainties were estimated to be $\pm 4\%$ for u' , $\pm 4\%$ for v' and w' , and $\pm 5\%$ for turbulent shear stresses such as $u'v'$. For rms velocities and shear stresses, percentages were based on maximum magnitude observed with each respective variable.

Results and Discussion

First presented is thermal field and flowfield data for the low freestream turbulence intensity case of $Tu_\infty = 0.5\%$. Comparison is made between apparent position of the jet, as indicated by flow fields, and time-mean height of the coolant core, as indicated by maximum θ . The comparison is especially of interest at $M = 3$

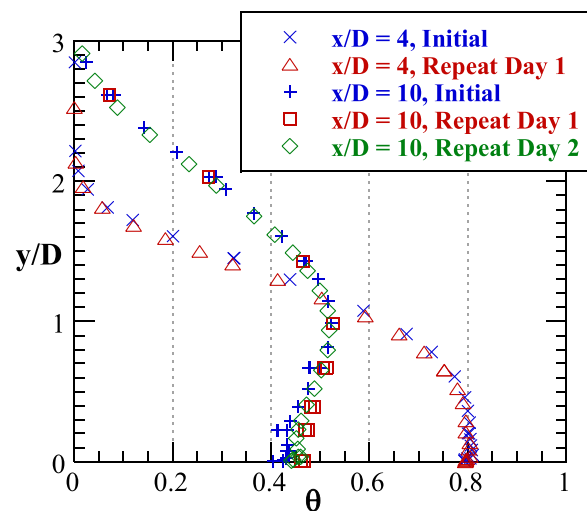


Fig. 4 Thermal field profiles showing repeatability for two streamwise locations in the centerline plane. Data are for shaped holes of a separate study at $Tu_\infty = 0.5\%$, $M = 3.0$.

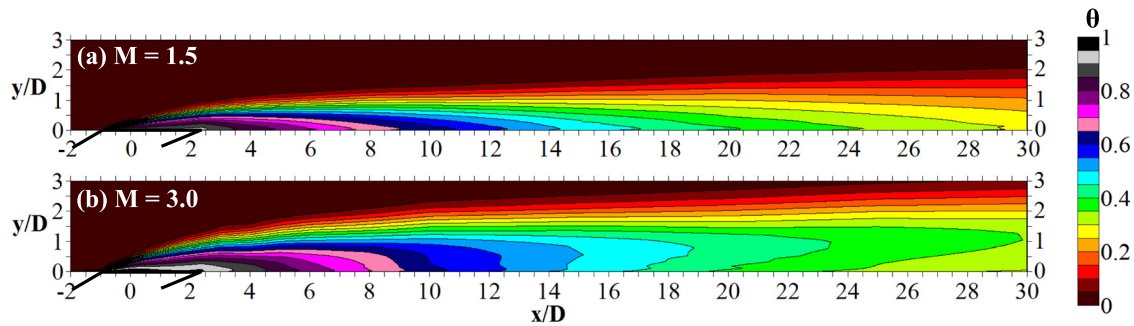


Fig. 5 Thermal field contours in the $z/D = 0$ centerline plane at $Tu_\infty = 0.5\%$ for blowing ratios of (a) $M = 1.5$ and (b) $M = 3.0$

where peaks in mean velocity occurred significantly above the wall. Subsequently, thermal field and then flowfield data are presented for the high freestream turbulence intensity case of $Tu_\infty = 13.2\%$.

Low Freestream Turbulence Intensity Results. Thermal fields in the centerline plane at blowing ratios of $M = 1.5$ and 3 and $Tu_\infty = 0.5\%$ are presented Figs. 5(a)–5(b). At $M = 1.5$, the time-mean coolant jet remained on the wall throughout the measurement domain, reaching a height of $y/D = 2.1$ at 30 diameters downstream of the hole centerline breakout. At $M = 3$, the coolant jet was also initially attached to the wall but exhibited maximum coolant concentration off the wall starting at $x/D = 14$. At $x/D = 30$, the top of the jet had reached a height of $y/D = 3.1$ and highest θ occurred at $y/D = 1$, off the wall.

Such delayed liftoff has not been previously reported in literature for either shaped holes ([5]) or cylindrical holes ([2]). The diffused outlet of shaped holes generally promotes jet attachment since the outlet slows coolant relative to velocity which would occur at a cylindrical hole exit. Past shaped hole studies, however,

have still shown presence of a counter-rotating vortex pair (CRVP) that lifts coolant away from the wall [11]. In Fig. 5(b), coolant liftoff was delayed to $x/D = 14$ because forward expansion of the outlet (β_{fwd}) lowered the effective injection angle and because coolant was laterally spread over the flat trailing edge of the hole. The CRVP brought mainstream fluid underneath sides of the coolant jet but downstream distance was required for this mainstream incursion to reach the $z/D = 0$ centerline. Kohli and Bogard [5] did not observe such liftoff in their thermal field measurements with shaped holes, likely due to the low blowing ratio ($M \leq 0.8$) and no measurements being downstream of their $x/D = 10$.

Vertical profiles of thermal and flowfield variables at the $M = 1.5$ and 3 conditions are shown in Figs. 6(a)–6(h). Data are from two stations in the centerline plane, $x/D = 1$ and 8. For each instance, dotted horizontal lines across the plots denote height at which coolant concentration fell below $\theta = 0.05$, an indicator of the coolant jet height. Also, for the $x/D = 8$ station which was downstream of the hole, measured adiabatic effectiveness (η) is plotted with θ , showing good agreement between the measures.

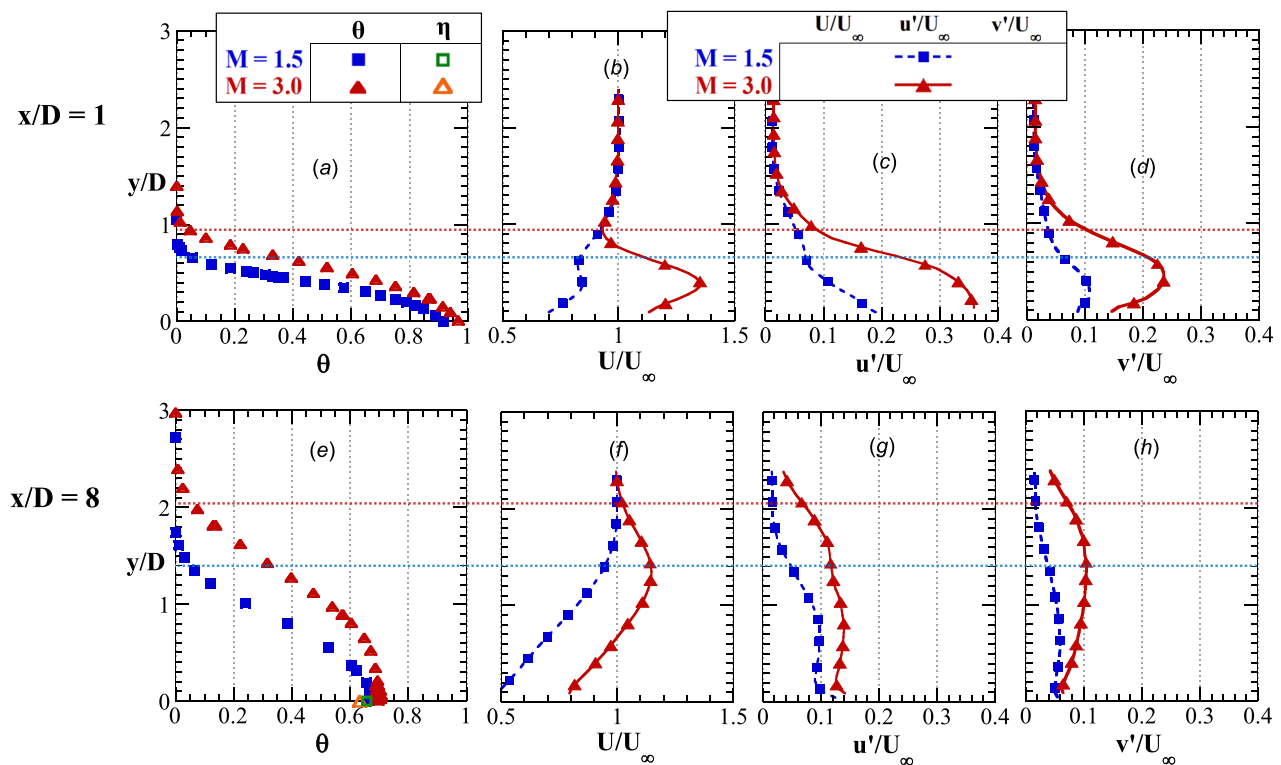


Fig. 6 Thermal field and flowfield profiles at $Tu_\infty = 0.5\%$ for $M = 1.5$ and 3 in the centerline plane at (a–d) $x/D = 1$ and (e–h) $x/D = 8$

At $x/D = 1$, in Figs. 6(a)–6(d), the jet was exiting the shaped hole diffused outlet. Consequently, the vertical temperature (θ) profile extended only slightly higher at this position for the $M = 3$ jet as compared to the $M = 1.5$ jet. Clear differences between $M = 1.5$ and 3 were seen in the profiles of mean streamwise velocity. At $M = 1.5$, the jet exited the hole with velocity lower than that of the freestream, while at $M = 3$, the jet had greater velocity than the freestream. Note the lines of $\theta = 0.05$ intersected mean velocity profiles approximately where the velocities returned to values consistent with the approach boundary layer. Such correspondence between time-mean temperature and velocity was expected, since path of the coolant was dictated by the mean flowfield. Figs. 6(c) and 6(d) show profiles of rms velocity fluctuations. It was difficult to judge jet height from these rms profiles due to their smooth, gradual changes with y/D height above the wall.

The profiles at $x/D = 8$ emphasize the same points and are shown in Figs. 6(e)–6(h). Thermal field profiles show that the $M = 3$ jet extended higher into the mainstream than the $M = 1.5$ jet. For $M = 3$, both the thermal field reached $\theta = 0.05$ and the mean velocity asymptotically reached $U/U_\infty = 1$ at the same height, $y/D = 2$. This agreement for the top edge of the jet again was consistent with how coolant was transported primarily by mean-flow convection. Similar correspondence was hard to ascertain at $M = 1.5$ because U/U_∞ exhibited a monotonic profile. Profiles of rms velocity varied even more gradually than at $x/D = 1$ and therefore it was not feasible to relate these rms profiles to the $\theta = 0.05$ heights.

While θ and U/U_∞ profiles agreed on vertical extent of the coolant jet, the profiles did not agree on apparent position of the coolant jet “core.” At $x/D = 1$ and 8, the coolant was most concentrated at $y/D = 0$ as seen in the thermal field profiles of Figs. 6(a) and 6(e). By contrast, peaks in mean streamwise velocity in Figs. 6(b) and 6(f) occurred off the wall. Therefore, flowfield data indicated vertical extent of the region containing the coolant jet but provided little information on relative coolant concentrations within this region.

High Freestream Turbulence Intensity Results. Thermal fields were measured for the blowing ratio $M = 3$ at $Tu_\infty = 13.2\%$. Contours in the centerline plane are shown in Fig. 7. For reference, dashed lines show contour levels of $\theta = 0.05$, 0.40, and 0.60 from the corresponding $M = 3$ low freestream turbulence case, which was shown in Fig. 5(b).

Contours of θ were significantly different between the low and high freestream turbulence cases. At high freestream turbulence, the jet was more diluted than at low freestream turbulence, apparent from how $\theta = 0.40$ and $\theta = 0.60$ contour levels extended shorter distances downstream for $Tu_\infty = 13.2\%$ as compared to the $Tu_\infty = 0.5\%$ case. However, there was negligible change in location of the $\theta = 0.05$ level representing the top of the coolant jet.

Also apparent in Fig. 7 is that liftoff did not occur in the high freestream turbulence case. Absence of the delayed liftoff was due to strong dilution of coolant caused by freestream turbulence, rather than due to a significant change in dynamics of the

flowfield. Schroeder and Thole [11] previously showed that there were no significant differences in mean velocities between the low and high freestream turbulence cases. The CRVP was of similar size and had similar velocities between the $Tu_\infty = 0.5\%$ and 13.2% cases. Absence of detachment can be understood as follows: At low freestream turbulence intensity, the jet stayed coherent for long distances downstream and therefore the CRVP eventually brought mainstream fluid beneath the core of the coolant jet. Conversely, the high freestream turbulence intensity caused aggressive mixing between coolant and the mainstream, especially in the top and middle of the coolant jet where turbulent fluctuations were not damped by the wall. By the downstream position of $x/D = 14$, the jet was more dilute and less coherent than at $Tu_\infty = 0.5\%$. The CRVP was not able to bring appreciably warmer fluid beneath the already-dilute jet, so liftoff was not seen.

Vertical profiles of the thermal field and flowfield are plotted in Figs. 8(a)–8(h), similar to Figs. 6(a)–6(h) given for the low freestream turbulence cases. Trends were similar to those seen with low freestream turbulence intensity. At each position, the thermal field reached $\theta = 0.05$ and streamwise velocity approached mainstream values at matching y/D height, indicating that vertical extent of the jet at $Tu_\infty = 13.2\%$ was still driven by the mean flowfield. Shape of the θ and U/U_∞ profiles again did not match, since highest θ occurred at the wall. Profiles of rms velocity fluctuations featured elevated values due to the turbulent freestream, and therefore rms velocity profiles did not sharply distinguish the jet/mainstream interface.

Thermal fields in the $x/D = 10$ lateral crossplane are compared between the low and high freestream turbulence cases in Figs. 9(a)–9(b). For both these $M = 3$ cases, the thermal field contours were widest above the wall, not at the wall. Therefore, tracing downward in y/D , the contour lines bent inward in the region nearest the wall, caused by the CRVP which gradually brought hot mainstream fluid underneath sides of the coolant jet. Just as Kohli and Bogard [5] did not observe delayed liftoff with their shaped holes, they also did not observe θ contour lines bending inward at the wall at the $x/D = 10$ crossplane or elsewhere. The difference between their study and the present study is again attributed to their lower flow rate, $M \leq 0.8$, accompanied by a weaker CRVP.

Figures 9(a)–9(b) show that elevated freestream turbulence caused increased dilution but also caused increased lateral dispersion of the coolant. For the low freestream turbulence case shown in Fig. 9(a), the highest coolant concentration was at the wall with maximum $\theta = 0.61$. The $\theta = 0.05$ contour level extended between $z/D = \pm 1.9$. Figure 9(b) shows that elevated freestream turbulence diluted the coolant such that maximum $\theta = 0.51$. Elevated freestream turbulence increased the lateral extent of $\theta = 0.05$ to $z/D = \pm 2.2$. In agreement with Fig. 7, the high freestream turbulence caused little increase in how high the $\theta = 0.05$ contour level extended above the wall.

The prevalence of dilution and of lateral dispersion with elevated freestream turbulence is illustrated by select adiabatic effectiveness contours in Fig. 10. Dashed lines represent η contour levels for the low freestream turbulence case, while solid lines represent η at high freestream turbulence. High freestream turbulence quickly penetrated coolant jets and diluted the jet core, as

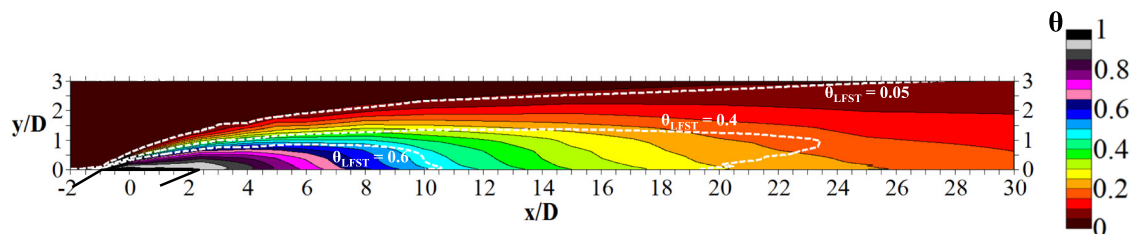


Fig. 7 Thermal field contours in the $z/D = 0$ centerline plane for $M = 3.0$ at $Tu_\infty = 13.2\%$. Labeled dashed white lines denote contour levels of $\theta_{LFST} = 0.05$, 0.40, and 0.60 for the corresponding case at low freestream turbulence intensity.

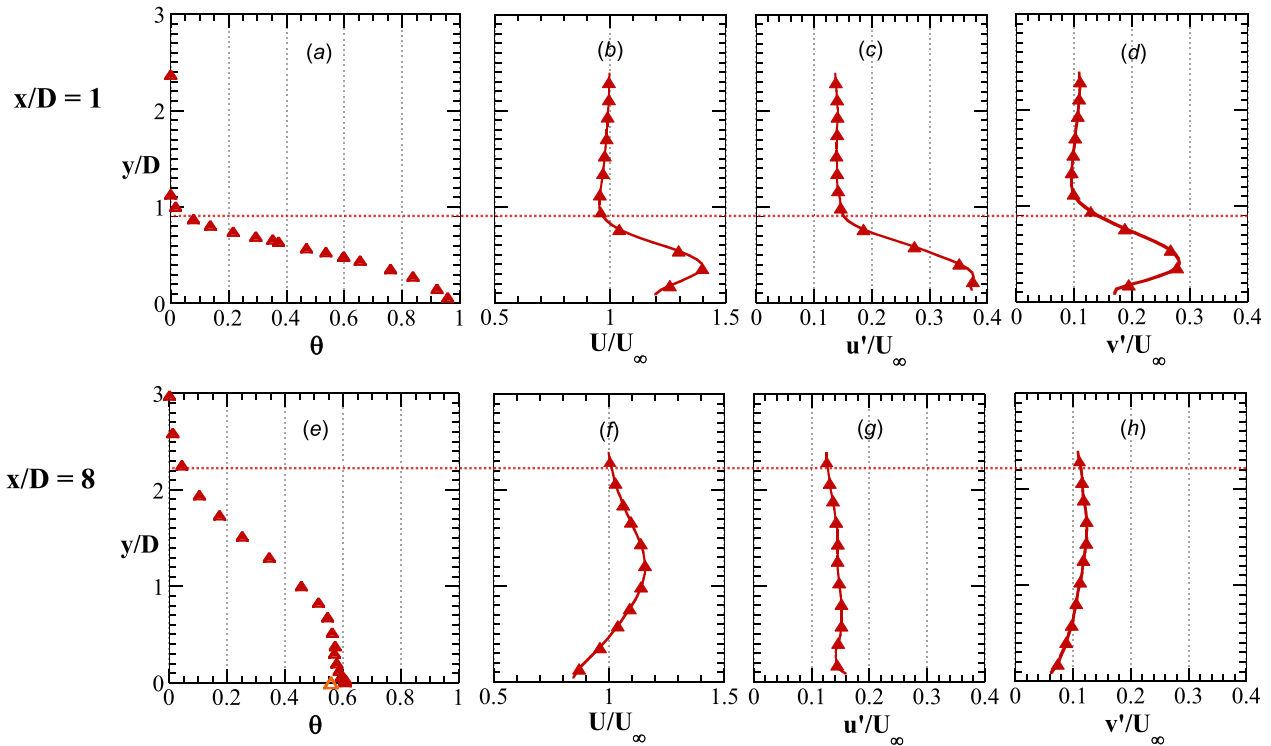


Fig. 8 Thermal field and flowfield profiles at $Tu_{\infty} = 13.2\%$ for $M = 3$ in the centerline plane at (a–d) $x/D = 1$ and (e–h) $x/D = 8$. Legend is the same as in Figs. 6(a)–6(h).

shown by how $\eta = 0.60$ levels extended shorter distances downstream of holes for the $Tu_{\infty} = 13.2\%$ case. At the same time, the high freestream turbulence increased spreading at the sides of the coolant jet. For these shaped holes spaced at $P/D = 6$, the $\eta = 0.05$ levels merged between adjacent jets by $x/D = 15$ for the $Tu_{\infty} = 13.2\%$ case.

Lateral Dispersion at High Freestream Turbulence. Thermal fields presented above showed that increased freestream turbulence caused increased lateral dispersion of coolant but

negligible increase in vertical dispersion of coolant. To illuminate mechanisms causing the difference between lateral and vertical dispersion, flowfields were examined in the $x/D = 4$ crossplane that was $1.6D$ downstream of the shaped hole trailing edge. Figures 11(a)–11(f) show contours of rms velocity fluctuations at $M = 3$, comparing u' , v' , and w' between the low and high freestream turbulence cases. Gray arrows overlaying the contours

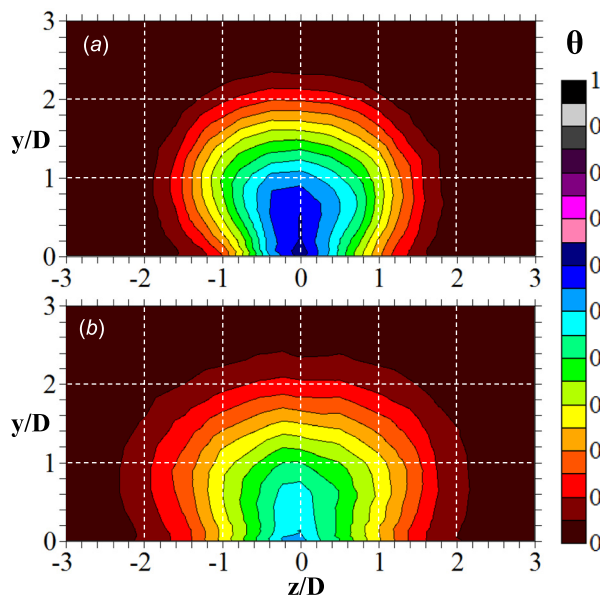


Fig. 9 Thermal field contours in the $x/D = 10$ crossplane at $M = 3.0$ with freestream turbulence intensities of (a) $Tu_{\infty} = 0.5\%$ and (b) $Tu_{\infty} = 13.2\%$

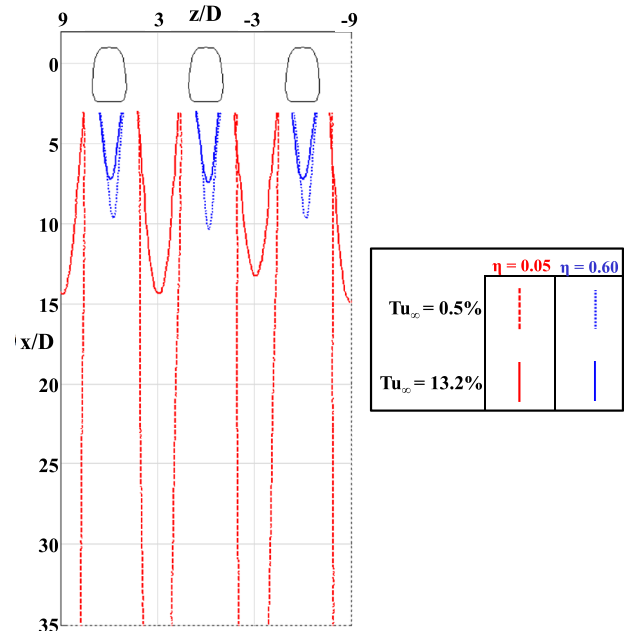


Fig. 10 Comparison of lateral spreading of $M = 3.0$ jets at free-stream turbulence of $Tu_{\infty} = 0.5\%$ (dashed lines) and $Tu_{\infty} = 13.2\%$ (solid lines) through plotting of $\eta = 0.05$ and 0.60 adiabatic effectiveness levels

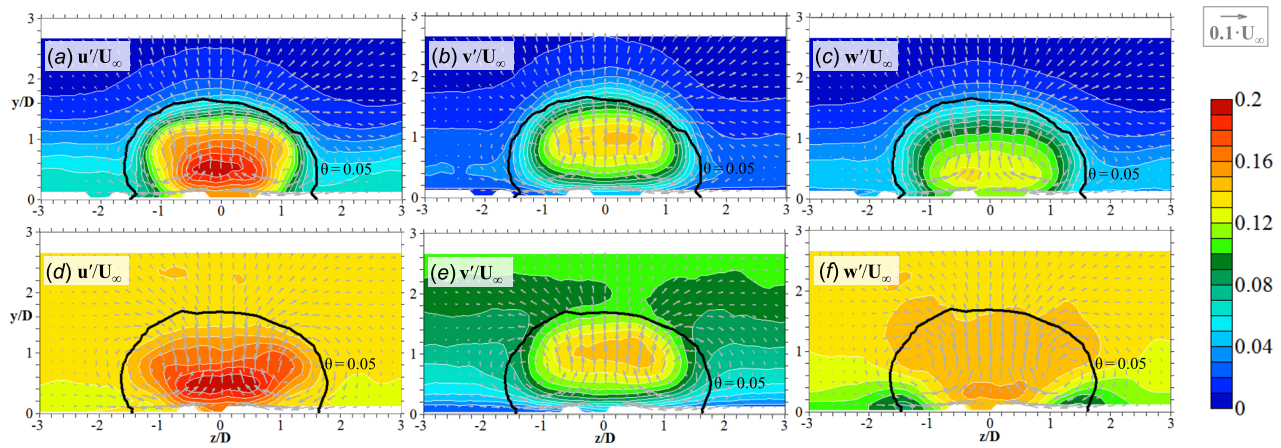


Fig. 11 Contours of rms velocity fluctuations at $M = 3.0$ in the $x/D = 4$ crossplane with (a–c) $Tu_\infty = 0.5\%$ and (d–f) $Tu_\infty = 13.2\%$. In-plane mean velocity is shown by gray arrows. The thermal field $\theta = 0.05$ contour is shown by the black curve.

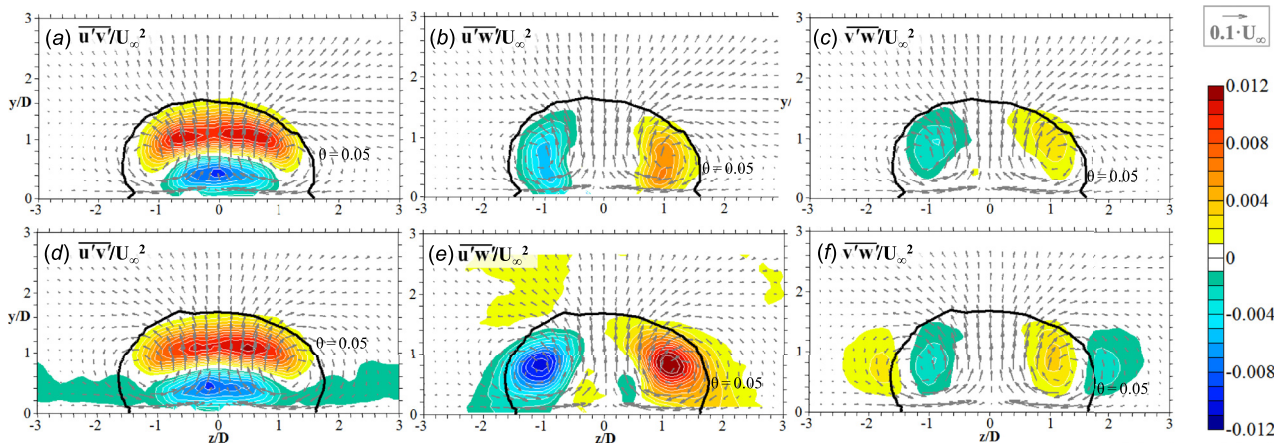


Fig. 12 Contours of turbulent shear stresses at $M = 3.0$ in the $x/D = 4$ crossplane with (a–c) $Tu_\infty = 0.5\%$ and (d–f) $Tu_\infty = 13.2\%$. In-plane mean velocity is shown by gray arrows. The thermal field $\theta = 0.05$ contour level is shown by the black curve.

show the in-plane mean velocity, revealing the counter-rotating vortex pair that was present. Also, overlaid is the $\theta = 0.05$ level representing the perimeter of the coolant jet. These perimeters, and θ contours overall (not shown for brevity), were similar in this $x/D = 4$ crossplane between the low and high freestream turbulence cases. Similar thermal fields here were expected, due to the crossplane being only a short distance downstream of the hole breakout.

Contours at low freestream turbulence intensity are plotted in Figs. 11(a)–11(c). With low freestream turbulence, the jet had higher turbulence intensity than the surrounding mainstream, resulting in regions of high turbulent fluctuations being well-contained within the $\theta = 0.05$ contour level. The only exception was that high levels of v'/U_∞ extended slightly beyond the top of the $\theta = 0.05$ contour level, indicating that coolant reached this height but was so dilute that concentration was below $\theta < 0.05$.

Contours at high freestream turbulence intensity are plotted in Figs. 11(d)–11(f). For the streamwise and lateral velocity components, fluctuations surrounding the coolant jet increased to $u'/U_\infty = w'/U_\infty = 0.14$ with this case of $Tu_\infty = 13.2\%$. Vertical velocity fluctuations also increased, reaching $v'/U_\infty = 0.10$ at the top of the coolant jet. Tracing slightly down sides of the coolant jet, u'/U_∞ and w'/U_∞ remained large but v'/U_∞ decreased due to the damping influence of the wall. Tracing down further, to the wall at $y/D = 0$, one finds that the minimum values of w'/U_∞ in Fig. 11(f) occurred where the $\theta = 0.05$ jet periphery met the wall. Lateral fluctuations here were $w'/U_\infty = 0.09$, similar to v'/U_∞ at

the top of the coolant jet. This near-wall region of minimum w'/U_∞ was due to acceleration of the lateral velocity component, which suppressed w' fluctuations. Acceleration was caused by the CRVP, which brought mainstream fluid (having low-magnitude lateral velocity) into the high-lateral-velocity region comprising the bottom section of the CRVP. While lateral fluctuations were damped by this phenomenon, lateral fluctuations were still greater than the $w'/U_\infty = 0.05$ present at the same location with $Tu_\infty = 0.5\%$ (Fig. 11(c)).

Comparable magnitude between v' at the coolant jet top and w' at coolant jet sides was a significant difference from the study by Cutbirth and Bogard [9], performed with compound-angle cylindrical holes on a vane pressure side. Their thermal fields showed, as in the present study, that high freestream turbulence caused increased lateral dispersion but not vertical dispersion of coolant. Cutbirth and Bogard attributed such dispersion to dominance of lateral fluctuations. Acceleration through the vane passage caused lateral fluctuations surrounding their coolant jet to be $w'/U_\infty = 0.20$, measured in a plane analogous to the $x/D = 4$ plane of the present study. By comparison, other components were $u'/U_\infty = v'/U_\infty = 0.12$ around their coolant jet.

In the present study, turbulent shear stresses in the same $x/D = 4$ crossplane provide insight into why high freestream turbulence caused primarily lateral spreading of coolant, instead of both lateral and vertical spreading. Figures 12(a)–(c) show normalized contours of $\overline{u'v'}$, $\overline{u'w'}$, and $\overline{v'w'}$ in the crossplane with the $M = 3$ jet at $Tu_\infty = 0.5\%$. Figures 12(d)–12(f) show the

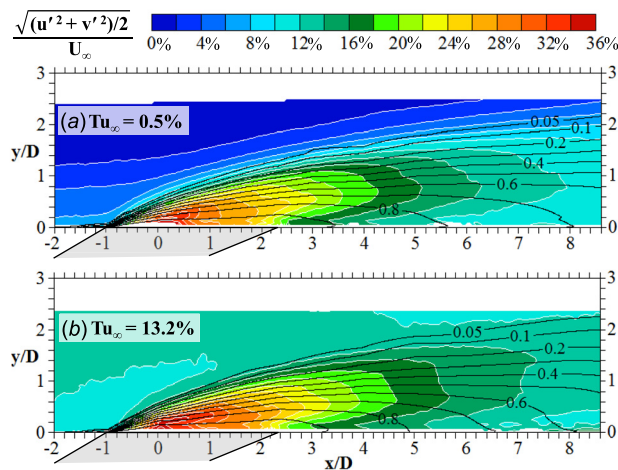


Fig. 13 Contours of turbulence intensity in the centerline plane, overlaid with contours levels of θ , at $M = 3.0$ with free-stream turbulence of (a) $Tu_\infty = 0.5\%$ and (b) $Tu_\infty = 13.2\%$

corresponding contours at $Tu_\infty = 13.2\%$. Mean in-plane velocities and the $\theta = 0.05$ jet periphery are overlaid as in Figs. 11(a)–11(f). Figures 12(a) and 12(d) compare $u'v'$ between the low and high freestream turbulence cases. For both freestream turbulence intensities, the upper half of the $\theta > 0.05$ region had positive $\overline{u'v'}$ consistent with momentum transport by turbulent viscosity. Packets of fluid originating at the center of the jet had high u -velocities. Such packets possessing higher-than-average vertical velocity brought fast-moving $M = 3$ coolant toward the top boundary of the jet, contributing to positive $\overline{u'v'}$. The region of positive $\overline{u'v'}$ decayed toward zero before encountering the $\theta = 0.05$ periphery, indicating that packets of concentrated coolant rarely made excursions far above the jet. The region of positive $\overline{u'v'}$ had similar magnitude and similar vertical extent between the $Tu_\infty = 0.5\%$ and 13.2% cases, showing that large eddies of the 13.2% free-stream turbulence did little to modify the dispersion occurring at the top of the coolant jet.

Freestream turbulence did make a difference in dispersion at sides of the coolant jet, as contours of $\overline{u'w'}$ show. In Fig. 12(b), the regions of negative and positive $\overline{u'w'}$ at the respective left and right sides of the jet were contained within the $\theta > 0.05$ region, just as with positive $\overline{u'v'}$ in Fig. 12(a). Such behavior was expected for low freestream turbulence, since turbulent fluctuations associated with the jet would not extend beyond the well-defined jet/mainstream shear layer. The patterns were different for the $Tu_\infty = 13.2\%$ case in Fig. 12(e). With high freestream turbulence, magnitudes of $\overline{u'w'}$ were increased in the left and right regions relative to the $Tu_\infty = 0.5\%$ case. The left and right regions also extended laterally beyond the $\theta = 0.05$ periphery, to $z/D = -2.3/2.6$. Note that lateral extent was greatest at $y/D = 0$. Wider $\overline{u'w'}$ patterns with $Tu_\infty = 13.2\%$ were due to instances where the coolant jet was swept by downward-moving eddies from the freestream turbulence. When these eddies started to feel impaction with the wall they deflected laterally, thereby contributing to much wider regions of nonzero $\overline{u'w'}$ than seen at $Tu_\infty = 0.5\%$. This influence of the wall on freestream eddies was the reason why elevated freestream turbulence preferentially augmented the lateral dispersion of coolant as compared to vertical dispersion. Unlike at the top of the jet, at sides of the jet, the eddies from freestream turbulence did indeed modify the dispersion behavior.

The third turbulent shear stress, $\overline{v'w'}$, is compared between low and high freestream turbulence cases in Figs. 12(c) and 12(f). Non-zero regions of $\overline{v'w'}$ occurred beyond lateral sides of the coolant jet at $Tu_\infty = 13.2\%$ but not at $Tu_\infty = 0.5\%$, which further

confirmed that the wall was preferentially directing turbulent eddies laterally.

Increased lateral dispersion with high freestream turbulence was mainly due to influence of the wall on eddies. However, changes in the distribution of turbulence within the jet caused dilution of coolant that was also a contributing factor to dominance of lateral dispersion. Figures 13(a)–13(b) compare turbulence intensity measured in the centerline plane at $Tu_\infty = 0.5\%$ and 13.2% . Thermal field contours at intervals of $\Delta\theta = 0.10$ are overlaid, with the $\theta = 0.05$ level included as well. Outside the jet, Figs. 13(a)–13(b) show increased turbulence with the elevation of freestream turbulence intensity to $Tu_\infty = 13.2\%$. Within the jet, the region where turbulence intensity increased most was the upper portion of the developed jet at several diameters downstream of the hole (past $x/D = 4$). This increase is evident, for example, from tracing upward at $x/D = 7$: in Fig. 13(a) the turbulence intensity decreases as one traces from the lower to the upper portion of the jet, while in Fig. 13(b), the turbulence intensity begins one contour level higher than at $Tu_\infty = 0.5\%$ but then remains high in the upper portion of the jet. The higher turbulence intensity in the upper part of the jet for the $Tu_\infty = 13.2\%$ case was not accompanied by significant change in contour levels of low θ representing the top edge of the jet. (Note that θ did decrease in regions closer to the wall with the elevation of freestream turbulence.) Elevated freestream turbulence caused mixing in the jet such that packets of cooler fluid dispersed upward were already dilute and therefore did not contribute to increased height of the $\theta = 0.05$ level from the $Tu_\infty = 0.5\%$ to the 13.2% case. A similar situation of unchanging- θ at the jet periphery was observed in the high freestream turbulence study of Kohli and Bogard [8] for a position 3D downstream of their cylindrical holes.

With elevation of freestream turbulence intensity from 0.5% to 13.2% , the constant θ at the top of the jet and the constant $\overline{u'v'}$ contained within the jet (Figs. 12(a) and 12(d)) were related effects. At the top of the coolant jet, instantaneous coolant concentrations and instantaneous fluid packets bearing high u -velocities representative of the jet were so dilute that they both made little contribution in the time-mean, even when freestream eddies swept the coolant upward out of the jet. Therefore, the high freestream turbulence caused increased lateral spreading of coolant without similar vertical spreading for two reasons: (1) eddies near the wall were preferentially directed laterally and (2) coolant subjected to these lateral fluctuations was more concentrated than coolant dispersed vertically out the top of the jet.

Conclusions

Thermal fields were measured for jets from shaped holes at high blowing ratios, at low and high freestream turbulence intensities of 0.5% and 13.2% . With low freestream turbulence, the jets penetrated farther into the mainstream with increased blowing ratio. At $M = 3$, the highest blowing ratio tested, the jet was attached to the wall as it exited the hole but farther downstream the jet lifted away from the wall due to action of the counter-rotating vortex pair.

The delayed liftoff observed at low freestream turbulence intensity was not observed with high freestream turbulence, due to strong dilution of the coolant jet by freestream turbulence. The main effects of high freestream turbulence were dilution of the coolant jet and increased lateral dispersion of coolant, as seen in thermal field and adiabatic effectiveness measurements. Thermal fields showed that high freestream turbulence caused little increase in vertical dispersion of the coolant jets.

Flowfields measured at the same conditions were compared to thermal field measurements but correlations were not found between flowfield variables and the distribution of coolant within jets. Turbulent shear stresses, however, did reveal reasons for the preferential lateral dispersion of coolant by elevated freestream turbulence. While the elevated turbulence did impose similar-magnitude vertical and lateral velocity fluctuations, coolant was

dispersed more in the lateral direction because of low coolant concentration at the top of the jet and because turbulent eddies containing the more-concentrated coolant were preferentially directed laterally by the wall.

The present study provides new information on dynamics of film cooling from shaped holes. Experimental data on phenomena such as delayed liftoff of jets and near-wall strengthening of lateral dispersion can lead to improved correlations and turbulence models used by designers for predicting shaped hole performance.

Acknowledgment

Support for this study was provided by the NASA Aeronautics Scholarship Program under Grant No. NNX14AE97H. The authors are grateful for this support and would like to thank James Heidmann and Mark Celestina at NASA for their guidance.

Nomenclature

A = hole cross-sectional area
 AR = area ratio, $A_{\text{exit}}/A_{\text{inlet}}$
 b = diameter of turbulence grid bars
 c_f = skin friction coefficient, measured experimentally
 $c_{f,0}$ = flat plate correlation c_f , $0.036 \text{Re}_{\delta_2}^{-0.3}$ (for $\text{Re}_{\delta_2} < 3000$) [15]
 $CRVP$ = counter-rotating vortex pair
 d_p = diameter of seeding particle
 D = diameter of film cooling holes
 DR = density ratio, ρ_c/ρ_∞
 H = boundary layer shape factor
 I = momentum flux ratio, $\rho_c U_c^2 / \rho_\infty U_\infty^2$
 k = thermal conductivity
 L = hole length
 \dot{m}_c = coolant mass flow rate
 M = blowing ratio, $\rho_c U_c / \rho_\infty U_\infty = (\dot{m}_c / A_c) / \rho_\infty U_\infty$
 P = lateral distance between holes, pitch
 PIV = particle image velocimetry
 Re = Reynolds number ($\text{Re}_{\delta_2} = \delta_2 U_\infty / \nu_\infty$)
 Stk = Stokes number, $\rho_p d_p^2 U_c / 18 \rho \nu D = (\rho_p d_p^2 / 18 \rho \nu) (D / U_c)$
 T = temperature
 Tu_∞ = freestream turbulence intensity, $\sqrt{(u'_{\infty}^2 + v'_{\infty}^2) / 2} / U_\infty$
 U_c = coolant area-average velocity in metering section
 U_∞ = mainstream mean velocity
 u, v, w = x-, y-, and z- velocities
 $\overline{u'v'}$ = streamwise-vertical component of turbulent shear stress
 $\overline{u'w'}$ = streamwise-lateral component of turbulent shear stress
 $\overline{v'w'}$ = vertical-lateral component of turbulent shear stress
 x, y, z = position, from origin at hole centerline breakout

Greek Symbols

α = hole injection angle
 β = expansion angle for diffused outlet
 δ_2 = boundary layer momentum thickness
 η = local adiabatic effectiveness, $(T_\infty - T_{aw}) / (T_\infty - T_c)$

θ = nondimensional fluid temperature, $(T_\infty - T) / (T_\infty - T_c)$
 Λ_x = integral length scale of freestream turbulence
 ν = kinematic viscosity
 ρ = fluid density

Subscripts

aw = adiabatic wall
 c = coolant, at hole inlet
 eff = effective, based on area at hole exit plane
 $exit$ = exit plane of the film cooling hole, per Fig. 2
 fwd = forward expansion of shaped hole
 $inlet$ = inlet plane of the film cooling hole, per Fig. 2
 lat = lateral expansion of shaped hole (half-angle)
 m = metering section
 p = seeding particle (DEHS droplet)
 ∞ = mainstream

Superscript

' = fluctuating/rms value

References

- [1] Bunker, R. S., 2005, "A Review of Shaped Hole Turbine Film Cooling Technology," *ASME J. Heat Transfer*, **127**(4), pp. 441–453.
- [2] Thole, K. A., Sinha, A. K., Bogard, D. G., and Crawford, M. E., 1992, "Mean Temperature Measurements of Jets With a Crossflow for Gas Turbine Film Cooling Application," *Rotating Machinery Transport Phenomena*, J. H. Kim, and W. J. Yang, ed., Hemisphere, New York.
- [3] Heneka, C., Schulz, A., Bauer, H., Heselhaus, A., and Crawford, M. E., 2012, "Film Cooling Performance of Sharp Edged Diffuser Holes With Lateral Inclination," *ASME J. Turbomach.*, **134**(4), p. 041015.
- [4] Colban, W., Thole, K. A., and Bogard, D., 2011, "A Film Cooling Correlation for Shaped Holes on a Flat-Plate Surface," *ASME J. Turbomach.*, **133**(1), p. 011002.
- [5] Kohli, A., and Bogard, D. G., 1999, "Effects of Hole Shape on Film Cooling With Large Angle Injection," *ASME Paper No. 99-GT-165*.
- [6] Takeishi, K., Kitamura, T., Komiyama, M., Oda, Y., and Mori, S., 2009, "Study on the Thermal and Flow Fields of Shaped Film Cooling Holes," Turbine-09, presented at Int'l Symposium on Heat Transfer in Gas Turbine Systems in Antalya, Turkey, Aug. 9–14, pp. 1–15.
- [7] Funazaki, K., Nakata, R., Kawabata, H., Tagawa, H., and Horiuchi, Y., 2014, "Improvement of Flat-Plate Film Cooling Performance by Double Flow Control Devices—Part I: Investigations on Capability of a Base-Type Device," *ASME Paper No. GT2014-25751*.
- [8] Kohli, A., and Bogard, D. G., 1998, "Effects of Very High Freestream Turbulence on the Jet-Mainstream Interaction in a Film Cooling Flow," *ASME J. Turbomach.*, **120**(3), pp. 785–790.
- [9] Cutbirth, J. M., and Bogard, D. G., 2002, "Evaluation of Pressure Side Film Cooling With Flow and Thermal Field Measurements—Part II: Turbulence Effects," *ASME J. Turbomach.*, **124**(4), pp. 678–685.
- [10] Schroeder, R. P., and Thole, K. A., 2014, "Adiabatic Effectiveness Measurements for a Baseline Shaped Film Cooling Hole," *ASME Paper No. GT2014-25992*.
- [11] Schroeder, R. P., and Thole, K. A., 2016, "Effect of High Freestream Turbulence on Flowfields of Shaped Film Cooling Holes," *ASME J. Turbomach.*, **138**(9), p. 091001.
- [12] Eberly, M. K., and Thole, K. A., 2014, "Time-Resolved Film Cooling Flows at High and Low Density Ratios," *ASME J. Turbomach.*, **136**(6), p. 061003.
- [13] LaVision, 2014, "Product Manual for DaVis 8.2.1.48998: FlowMaster," LaVision GmbH, Göttingen, Germany, Item No. 1105011-4.
- [14] Figliola, R. S., and Beasley, D. E., 2006, *Theory and Design for Mechanical Measurements*, Wiley, Hoboken, NJ.
- [15] Bogard, D. G., and Thole, K. A., 1998, "Wall-Bounded Turbulent Flows," *CRC Handbook of Fluid Dynamics*, Sec. 13.5, CRC Press, Boca Raton, FL, pp. 13.49–13.63.